



Article scientifique

Article

2013

Published version

Open Access

This is the published version of the publication, made available in accordance with the publisher's policy.

---

## 3D Prior Image Constrained Projection Completion for X-ray CT Metal Artifact Reduction

---

Mehranian, Abolfazl; Ay, Mohammad Reza; Rahmim, Arman; Zaidi, Habib

### How to cite

MEHRANIAN, Abolfazl et al. 3D Prior Image Constrained Projection Completion for X-ray CT Metal Artifact Reduction. In: IEEE transactions on nuclear science, 2013, vol. 60, n° 5, p. 3318–3332. doi: 10.1109/TNS.2013.2275919

This publication URL: <https://archive-ouverte.unige.ch/unige:40373>

Publication DOI: [10.1109/TNS.2013.2275919](https://doi.org/10.1109/TNS.2013.2275919)

# 3D Prior Image Constrained Projection Completion for X-ray CT Metal Artifact Reduction

Abolfazl Mehranian, Mohammad Reza Ay, *Member, IEEE*, Arman Rahmim, *Senior Member, IEEE*, and Habib Zaidi, *Senior Member, IEEE*

**Abstract**—The presence of metallic implants in the body of patients undergoing X-ray computed tomography (CT) examinations often results in severe streaking artifacts that degrade image quality. In this work, we propose a new metal artifact reduction (MAR) algorithm for 2D fan-beam and 3D cone-beam CT based on the maximum a posteriori (MAP) completion of the projections corrupted by metallic implants. In this algorithm, the prior knowledge obtained from a tissue-classified prior image is exploited in the completion of missing projections and incorporated into a new prior potential function. The prior is especially designed to exploit and promote the sparsity of a residual projection (sinogram) dataset obtained from the subtraction of the unknown target dataset from the projection dataset of the tissue-classified prior image. The MAP completion is formulated as an equality-constrained convex optimization and solved using an accelerated projected gradient algorithm. The performance of the proposed algorithm is compared with two state-of-the-art algorithms, namely 3D triangulated linear interpolation (LI) and normalized metal artifact reduction (NMAR) algorithm using simulated and clinical studies. The simulations targeting artifact reduction in 2D fan-beam and 3D cone-beam CT demonstrate that our algorithm can outperform its counterparts, particularly in cone-beam CT. In the clinical datasets, the performance of the proposed algorithm was subjectively and objectively compared in terms of metal artifact reduction of a sequence of 2D CT slices. The clinical results show that the proposed algorithm effectively reduces metal artifacts without introducing new artifacts due to erroneous interpolation and normalization as in the case of LI and NMAR algorithms.

**Index Terms**—Metal artifact reduction, prior image, X-ray CT, 3D projection completion.

## I. INTRODUCTION

X-RAY computed tomography (CT) has experienced considerable technical advances over the past two decades and has now emerged as a leading cross-sectional imaging

Manuscript received January 21, 2013; revised July 15, 2013; accepted July 29, 2013. Date of publication September 04, 2013; date of current version October 09, 2013. This work was supported in part by the Swiss National Science Foundation under grant SNSF 31003A-135576, in part by the Indo-Swiss Joint Research Programme ISJRP 138866, and in part by Geneva University Hospital under Grant PRD 11-II-1.

A. Mehranian is with the Division of Nuclear Medicine and Molecular Imaging, Geneva University Hospital, CH-1211 Geneva, Switzerland (e-mail: mehrani1@etu.unige.ch).

M. R. Ay is with the Department of Medical Physics and Biomedical Engineering and the Research Center for Molecular and Cellular Imaging, Tehran University of Medical Sciences, Tehran, Iran (e-mail: mohammadreza\_ay@sina.tums.ac.ir).

A. Rahmim is with the Department of Radiology, School of Medicine, Johns Hopkins University, Baltimore, MD 21287 USA (e-mail: arahmim1@jhmi.edu).

H. Zaidi is with the Division of Nuclear Medicine and Molecular Imaging, Geneva University Hospital, CH-1211 Geneva, Switzerland, the Neuroscience Center, Geneva University, Geneva, Switzerland, and also with the Department of Nuclear Medicine and Molecular Imaging, University of Groningen, University Medical Center Groningen, Groningen, Netherlands (e-mail: habib.zaidi@hcg.ch).

Color versions of one or more of the figures in this paper are available online at <http://ieeexplore.ieee.org>.

Digital Object Identifier 10.1109/TNS.2013.2275919

technique for various diagnostic and therapeutic applications. However, the appearance of streaking metal artifacts in CT images of patients bearing metallic implants can obscure crucial diagnostic information and therefore reduce image quality and the clinical relevance of this valuable imaging modality. As polychromatic X-ray beams used in CT pass through a patient, low energy (soft) X-ray photons, which are often of little importance to image formation, are preferentially absorbed to a greater extent than high energy photons. The outcome of this selective absorption is that patient's absorbed dose increases and the X-ray beam gets richer in high energy photons and thus becomes harder [1]. Due to this so-called beam hardening effect, the log-processed transmission data will no longer be a linear function of tissue thickness. In the presence of strongly attenuating objects, such as metallic implants, beam hardening and Compton scattering become so severe that the detectors sensing the implants get starved of photons, and thus the relevant projection data become corrupted and inconsistent. The filtered backprojection (FBP) reconstruction algorithm, which is widely used in CT image reconstruction, assumes a linear or monochromatic propagation model for the detected photons and, as such fails to consider the non-linear beam hardening and scattering effects [2]. Consequently, the reconstructed images exhibit cupping artifacts, declined CT numbers behind bony structures [3] and contrast-enhanced regions [4], and streaking artifacts around metallic objects [5]. Most current generation commercial CT scanners, however, apply first-order beam hardening correction (water correction) algorithms to compensate for beam hardening, but due to the incapability of these algorithms to calibrate the beam hardening of high-Z materials, streaking artifacts still appear in the reconstructed images. The dark and bright streaking artifacts can obscure pathologic lesions and degrade the radiological manifestation of the surrounding tissues. Consequently, since the past three decades, extensive efforts have been directed toward developing efficient metal artifact reduction (MAR) algorithms in order to compensate for the corrupted and missing projection data and hence to improve the diagnostic quality and confidence of CT imaging.

Typically, MAR algorithms comprise two steps: a) metal trace identification, in which the projections corrupted by metallic implants are identified and b) artifact reduction, through which the identified missing projections are compensated for or treated in such a way that the associated streaking artifacts are mitigated. Metal traces are conventionally identified by segmentation of metallic implants in FBP reconstructed images using thresholding [5]–[7] or clustering techniques [8], [9] followed by reprojection of the obtained *metal-only* images onto the projection or sinogram domain. Other approaches are

based on segmentation of metal traces directly in raw sinogram data using active contours [10], curve detection [11] and Markov random field (MRF) [12] techniques. More recently, hybrids of these two approaches have also been proposed using iterative metal-only image reconstruction and segmentation [13]–[16]. The second step of MAR methods has been mainly explored by two classes of algorithms: projection completion and iterative image reconstruction.

Projection completion aims at interpolating the missing projections from their neighbors through linear [5], cubic spline [6], [17], and wavelet [18] interpolations or iterative inpainting techniques using curvature-driven diffusion [19], [20], total variation (TV) [10], [21], [22] and wavelet regularization [23]. Other approaches rely on replacing the missing projections with the projections from nearby slices or opposite side angles [24], [25]. Bal and Spies proposed to replace the missing projections by the projections obtained from the forward projection of a tissue-classified CT image, namely tissue-class model or *prior* image [8]. The problem with this approach is that the prior sinogram projections over missing regions (metal traces) are not well fitted with the projections of the original sinogram in immediate neighboring regions and hence, there is always a risk for discontinuities and generation of new artifacts. Recently, Meyer *et al.* [26] proposed a promising method to solve this fitness problem. In this method, referred to as normalized MAR (NMAR), the original sinogram is normalized by the sinogram of prior image, thereby flattening neighboring projections. Then, the missing data are linearly interpolated and the resulting sinogram is de-normalized. Projection completion has also been combined with algorithms that exploit the information hidden in low- and high-pass filtered sinograms [27] or low- and high-pass filtered reconstructed images [28]. This class of algorithms is often fast and computationally appealing; however, if not efficiently implemented, these techniques might produce new artifacts. In fact, their efficiency depends on how robustly they can exploit the still available projection data or even a prior knowledge in the recovery of missing data.

On the other hand, iterative reconstruction algorithms establish another class of algorithms that, unlike FBP, attempt to frame the reconstruction problem in a way that more closely resembles reality. In their evolution from algebraic to model-based statistical reconstruction techniques, these algorithms have allowed for a rich description of physical and statistical mechanisms involved in the imaging process and also for incorporating a priori knowledge of the images to be reconstructed [29]. They can be adapted to missing data situations by down-weighting [30], [31] or ignoring [13], [32], [33] the contribution of the corrupted projections, or can be tailored to polychromatic propagation models in order to reduce both beam hardening and metallic artifacts [34], [35]. However, this class of algorithms cannot entirely eradicate severe metallic artifacts [36], hence their initiation [31], [37] and combination [38] with projection completion techniques have also been investigated. Despite their advantages and the development of GPU-based and parallelizable algorithms [2], iterative image reconstruction techniques are still memory-demanding and computationally intensive. To reduce the computational complexity of this class of MAR algorithms, Van Slambrouck *et al.* [40] proposed a

region-based iterative reconstruction method. In this method, a fully polychromatic reconstruction model is used for metallic regions, while a simpler monochromatic model is used for other regions. It is worth noting that model-based iterative algorithms have also been successfully applied for sinogram restoration and beam hardening correction [41], [42]. Interested readers are referred to a recent review on MAR algorithms [39].

In this study, we propose a three-dimensional (3D) projection completion MAR algorithm in a Bayesian framework for the maximum *a posteriori* (MAP) completion of missing projections. In this framework, we systematically exploit the side information obtained from a tissue-classified prior image and also prior knowledge about the unknown projections based on previous works in the framework of compressed sensing and sparse signal recovery. In this context, the prior knowledge that a target signal or solution is sparse (i.e. having many zero components) or has a sparse and/or compressible representation in a given transform domain is exploited to recover it from its samples or incomplete measurements. Chen *et al.* proposed a prior image constrained compressed sensing technique for reducing streaking artifacts in CT image reconstruction from undersampled projection angles [43]. In this technique, the target image is sparsified by subtraction from a prior image and then the subtracted image is further sparsified using a discrete gradient operator. Motivated by the concept of subtraction sparsification in the context of compressed sensing [43], [44] and prior image application in metal artifact reduction [8], [26], [45], we propose a new prior function to exploit i) the sparsity of a residual sinogram obtained from the subtraction of a target sinogram and a prior sinogram and ii) a sparsity-promoting diffusivity function defined on the prior sinogram for the recovery of missing projections. Furthermore, we extend the proposed MAP projection completion to three dimensions in order to interpolate the missing projections from all available projection data. The idea of 3D interpolation has previously been studied for recovery of missing projections in flat-panel cone beam CT [45] and in a sequence of 2D CT slices [46]. In the present work, we evaluate the performance of the proposed MAR algorithm in comparison with NMAR and a 3D linear interpolation algorithm implemented on a triangulated mesh grid using simulation and clinical studies and demonstrate that our MAR approach can potentially outperform the above state-of-the-art algorithms.

## II. MATERIALS AND METHODS

### A. Problem Formulation

Let  $\mathbf{x}_o \in \mathbb{R}^N$  denote an observed CT projection (sinogram) dataset with projections corrupted by metallic implants over the set  $\Omega \subset \{1, \dots, N\}$ , namely missing or metal-trace set. In the recovery of the underlying uncorrupted projection dataset,  $\mathbf{x}$ , we formulate the following forward model:

$$\mathbf{y} = \mathbf{H}\mathbf{x} + \mathbf{n} \quad (1)$$

where  $\mathbf{H} \in \mathbb{R}^{M \times N}$ ,  $M < N$ , is a lossy operator that removes the projections of  $\mathbf{x}$  over the set  $\Omega$ .  $\mathbf{y} \in \mathbb{R}^M$  is the observed dataset with removed or missing projections and  $\mathbf{n}$  represents zero-mean Gaussian white noise with variance  $\sigma^2$ . The matrix

$\mathbf{H}$  is constructed in two steps: i) an  $N \times N$  diagonal matrix is defined with zero and one diagonal values. The rows and columns along which this matrix is zero are indexed by the set  $\Omega$ . ii) The zero-rows of the matrix are then removed. In effect, the resulting  $M \times N$  matrix removes the elements of  $\mathbf{x}$  over the set  $\Omega$ . In (1), the system of equations is underdetermined and therefore has an infinite number of solutions. In order to regulate and confine the solution space, we follow a Bayesian estimation approach. In this approach, one aims at finding a solution that maximizes the *a posteriori* probability density of  $\mathbf{x}$  given  $\mathbf{y}$ , which according to Bays' rule is given by

$$P(\mathbf{x}|\mathbf{y}) \propto P(\mathbf{y}|\mathbf{x})P(\mathbf{x}) \quad (2)$$

where r.h.s densities are respectively the probability density of  $\mathbf{y}$  given  $\mathbf{x}$  and the prior probability density of  $\mathbf{x}$ . Since the density probability for the observation of  $\mathbf{y}$  given  $\mathbf{x}$  is the density for  $\mathbf{n} = \mathbf{y} - \mathbf{H}\mathbf{x}$ , we have

$$P(\mathbf{y}|\mathbf{x}) \sim e^{-\frac{1}{2\sigma^2}\|\mathbf{y}-\mathbf{H}\mathbf{x}\|^2} \quad (3)$$

where  $\|\mathbf{z}\| = \sqrt{\sum_i z_i^2}$ . In this framework, the unknown  $\mathbf{x}$  is treated as a stochastic quantity with a prior probability density,  $P(\mathbf{x}) \sim e^{-U(\mathbf{x})}$ , where  $U(\mathbf{x})$  is Gibbs or prior energy. This density is in fact used to impose our prior knowledge on the estimation. The MAP estimation is then obtained by maximizing  $P(\mathbf{x}|\mathbf{y})$  or equivalently minimizing the following a posteriori energy:

$$\hat{\mathbf{x}} = \operatorname{argmin}_{\mathbf{x}} \left\{ \frac{1}{2\sigma^2}\|\mathbf{y} - \mathbf{H}\mathbf{x}\|^2 + U(\mathbf{x}) \right\}. \quad (4)$$

In the above equation, the first term measures the proximity of  $\mathbf{x}$  to  $\mathbf{y}$  if observed through  $\mathbf{H}$ , while the second term enforces the compliance of  $\mathbf{x}$  to our prior knowledge. Generally, as the variance of noise decreases, the proximity of  $\mathbf{H}\mathbf{x}$  to  $\mathbf{y}$  increases. In the limit where no noise is introduced as  $\mathbf{H}$  operates on  $\mathbf{x}$  (as is the case in this work), the problem defined in (4) asymptotically reduces to the following constrained optimization problem:

$$\hat{\mathbf{x}} = \operatorname{argmin}_{\mathbf{x} \in \Theta} U(\mathbf{x}), \quad \Theta = \{\mathbf{x} \in \mathbb{R}^N | \mathbf{y} = \mathbf{H}\mathbf{x}\} \quad (5)$$

where  $\Theta$  is a constraint set inside which the linear set of equations  $\mathbf{y} = \mathbf{H}\mathbf{x}$  defines the feasible set of solutions. Geometrically speaking, this set appears as a hyperplane whose intersection with the ball of the prior  $U(\mathbf{x})$  defines the solution. Solving (5) is in fact achieved by decreasing the prior's energy until its ball last touches the hyperplane.

To impose our prior knowledge about the unknown  $\mathbf{x}$ , we employ a prior function whose gradient at point  $\mathbf{x}$  is defined as follows:

$$U' = \nabla^T (g(\|\nabla \mathbf{x}_p\|)) \nabla (\mathbf{x} - \alpha \mathbf{x}_p) \\ g(t) = \frac{1}{1 + \alpha \left(\frac{t}{\delta}\right)^2}, \quad (6)$$

where  $\nabla \in \mathbb{R}^{3N \times N}$  is a 3D derivative matrix (with symmetric boundary conditions) that approximates the gradient using first-order finite differences in horizontal, vertical and axial directions,  $\mathbf{x}_p$  is the sinogram of a tissue-classified prior image (prior

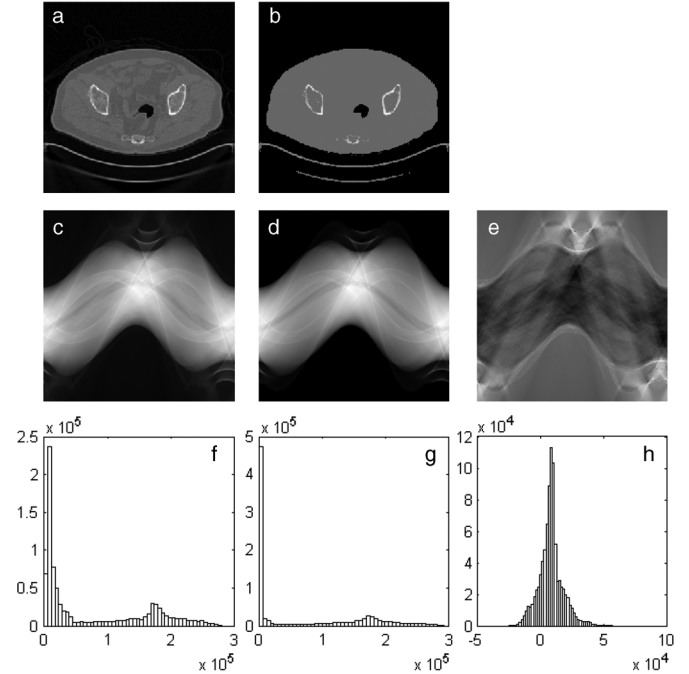


Fig. 1. Illustration of subtraction sparsification. (a)–(d) A target CT image and its tissue-classified prior image and their corresponding sinograms, respectively. (e) The sinogram obtained from the subtraction of the target and prior sinograms. (f–h) The histograms of the sinograms shown in (c)–(e) in 30 bins. The histograms show that sinogram subtraction gives rise to the compressibility of the target sinogram.

sinogram),  $g(t)$ ,  $\delta > 0$ , is a modified Perona-Malik diffusivity function [47] and  $\alpha \in [0, 1]$  is a relaxation parameter to weight the impact of the prior sinogram.

The proposed prior function exploits two types of side information i) the diffusion directions into missing regions obtained from the prior sinogram and ii) the sparsity or compressibility of the subtraction sinogram. Fig. 1 further illustrates the idea of subtraction sparsification. Figs. 1(a)–(e) show a target image and its tissue-classified prior image, their sinograms as well as the subtraction sinogram, respectively. In Figs. 1(f)–(h), the corresponding histograms of the sinograms are shown in 30 bins. As can be seen, the subtraction gives rise to the compressibility of the target sinogram. Therefore, the application of discrete gradient operator  $\nabla$  can promote the sparsity of the subtraction sinogram. In (6), when  $\alpha$  tends toward zero, the problem in (5) reduces to a constrained Tikhonov energy minimization. In Section II-C, we will elaborate the derivation of a prior image from an observed CT image with metal artifacts.

## B. The Optimization Algorithm

To solve the problem in (5), we follow an optimization transfer technique within the context of convex programming [48]. In this technique, the original objective function is iteratively substituted by a convex, easy-to-optimize surrogate function, which transfers its optimization to the objective function. Let us recast the problem in (5) into the following unconstrained problem:

$$\min_{\mathbf{x}} \{U(\mathbf{x}) + \iota_{\Theta}(\mathbf{x})\} \quad \iota_{\Theta}(\mathbf{x}) = \begin{cases} 0, & \mathbf{x} \in \Theta \\ \infty, & \mathbf{x} \notin \Theta \end{cases} \quad (7)$$

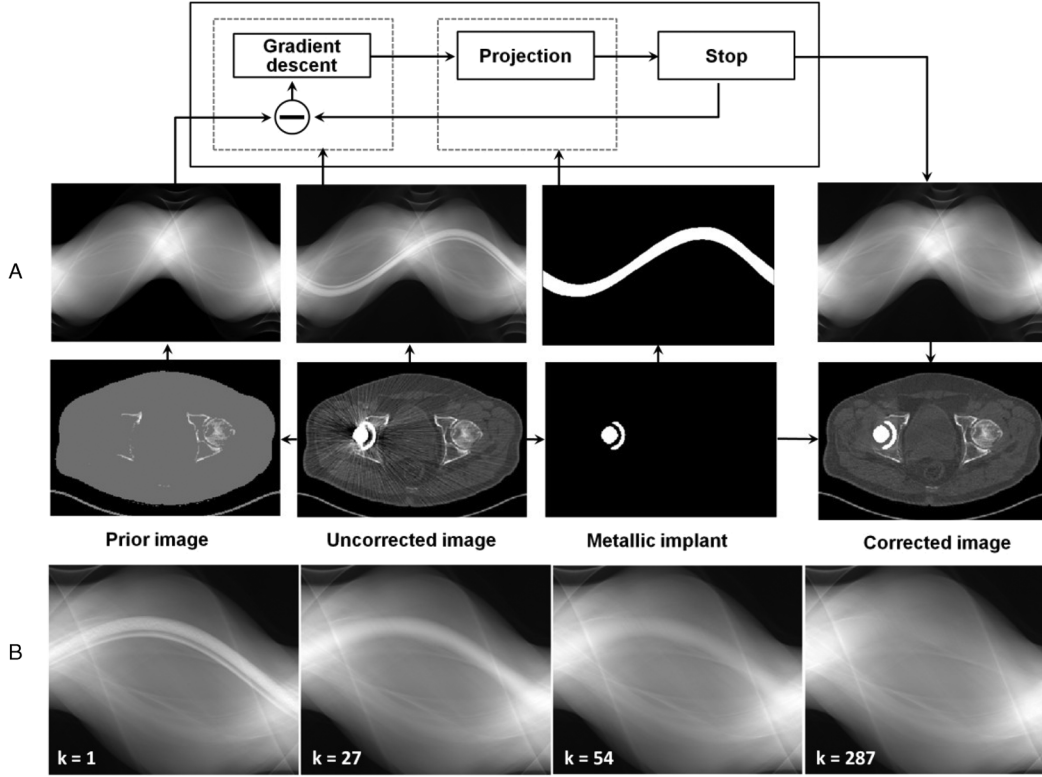


Fig. 2. A) Flowchart of the proposed algorithm. The uncorrected CT image is segmented to extract metallic implants and tissue-prior image. The sinogram of the images are fed into the algorithm, which consists of two main steps: i) gradient descent of a subtraction sinogram, obtained by subtracting the prior sinogram and estimated sinogram, and ii) a projection step in which the already known projections are inserted into the estimated sinogram. The corrected image is obtained by FBP reconstruction of the estimated sinogram and then metallic implants are added back to the image. Panel B) illustrates the recovery of corrupted projections as a function of the number of iterations ( $k$ ).

where  $\iota_{\Theta}$  is the indicator function of the set  $\Theta$ . To obtain a convex surrogate, we approximate the function  $U(\mathbf{x})$  at point

---

#### Algorithm 1 Prior Image Constrained Projection Completion

---

Choose:  $\delta, \tau, \alpha$  and  $\eta$ ; initialize:  $\mathbf{x}^{(-1)} = \mathbf{x}^{(0)} = \mathbf{x}_u, t^{(0)} = 1, k = 0$  and  $\mathbf{g} = (1 + \alpha(\|\nabla \mathbf{x}_p\|/\delta))^{-1}$ .

**While** ( $\|\mathbf{x}^{(k+1)} - \mathbf{x}^{(k)}\|/\|\mathbf{x}^{(k)}\| < \eta$ ) **do**,

- 1)  $t^{(k+1)} = (1/2)(1 + \sqrt{1 + 4(t^{(k)})^2})$ .
- 2)  $\tilde{\mathbf{x}} = \mathbf{x}^{(k)} + ((t^{(k)} - 1)/t^{(k+1)})(\mathbf{x}^{(k)} - \mathbf{x}^{(k-1)})$ .
- 3)  $\mathbf{x}^{(k+1)} = \text{proj}_{\iota_{\Theta}}(\tilde{\mathbf{x}} - \tau \nabla^T(\mathbf{g} \nabla(\mathbf{x}^{(k)} - \mathbf{x}_p)))$ .
- 4)  $k = k + 1$ .

**Output:**  $\mathbf{x}^{(k+1)}$ .

---

$\mathbf{x}^{(k)}$  using second-order Taylor expansion. Thus, the resulting surrogate reads

$$S(\mathbf{x}, \mathbf{x}^{(k)}) = U(\mathbf{x}^{(k)}) + U'(\mathbf{x} - \mathbf{x}^{(k)})^T + \frac{L}{2} \|\mathbf{x} - \mathbf{x}^{(k)}\|^2 + \iota_{\Theta}(\mathbf{x}) \quad (8)$$

where  $L$  is the Lipschitz constant of the gradient of the prior function. By completing the square, dropping terms independent of  $\mathbf{x}$  in (8) and letting  $\tau = 1/L$ , the solution then iteratively reads

$$\mathbf{x}^{(k+1)} = \underset{\mathbf{x}}{\text{argmin}} \left\{ \frac{1}{2\tau} \|\mathbf{x} - \mathbf{u}^{(k)}\|^2 + \iota_{\Theta}(\mathbf{x}) \right\} \triangleq \text{prox}_{\iota_{\Theta}}(\mathbf{u}^{(k)}) \quad (9)$$

<sup>1</sup> $\mathbf{x}_u$  and  $\mathbf{x}_p$  are uncorrected and prior sinograms.

where  $\mathbf{u}^{(k)} = \mathbf{x}^{(k)} - \tau U'(\mathbf{x}^{(k)})$  is a gradient descent with step size  $\tau$  and  $\text{prox}_{\iota_{\Theta}}(\cdot)$  is a proximal mapping associated with the function  $\iota_{\Theta}(\mathbf{x})$ . This algorithm is referred to as a proximal gradient algorithm [49]. Since  $\iota_{\Theta}(\mathbf{x})$  is an indicator function, the proximal mapping reduces to a projection onto the convex set (POCS)  $\Theta$ . For the constraint sets that are hyperplanes, the POCS step is achieved by the following algebraic reconstruction technique [50]:

$$\text{proj}_{\iota_{\Theta}}(\mathbf{u}^{(k)}) = \mathbf{u}^{(k)} + \mathbf{H}^T (\mathbf{y} + \mathbf{H} \mathbf{u}^{(k)}). \quad (10)$$

The above projector, in effect, inserts the already known projections from  $\mathbf{y}$  into  $\mathbf{u}^{(k)}$ . The Lipschitz constant  $L$  plays an important role in the convergence of gradient-based algorithms. According to Theorem 8.3 in [50], for a fixed step size,  $\tau$ , a gradient descent algorithm converges to the minimizer of a function if  $0 < \tau \leq (2/L)$ . As mentioned above, as  $\alpha \rightarrow 0$  in (6), the prior function becomes a Tikhonov function, whose Lipschitz constant is given by  $L_T = \lambda_{max}(\nabla^T \nabla)$ , where  $\lambda_{max}$  is the largest eigenvalue. This implies that the  $L$  constant of the proposed functional should be larger than  $L_T$ . Using the power iteration method or the result presented in Appendix B in [51], one can show that  $L_T \leq 8$  for 2D datasets and  $L_T \leq 12$  for 3D datasets. In this work, we improved the convergence rate of the optimization algorithm using Nesterov's acceleration [52]. To this end, Algorithm 1 summarizes the employed optimization algorithm whereas Fig. 2 shows the flowchart of the algorithm. In this algorithm, we declare the convergence of the algorithm when the relative difference between  $\mathbf{x}^{(k+1)}$  and  $\mathbf{x}^{(k)}$

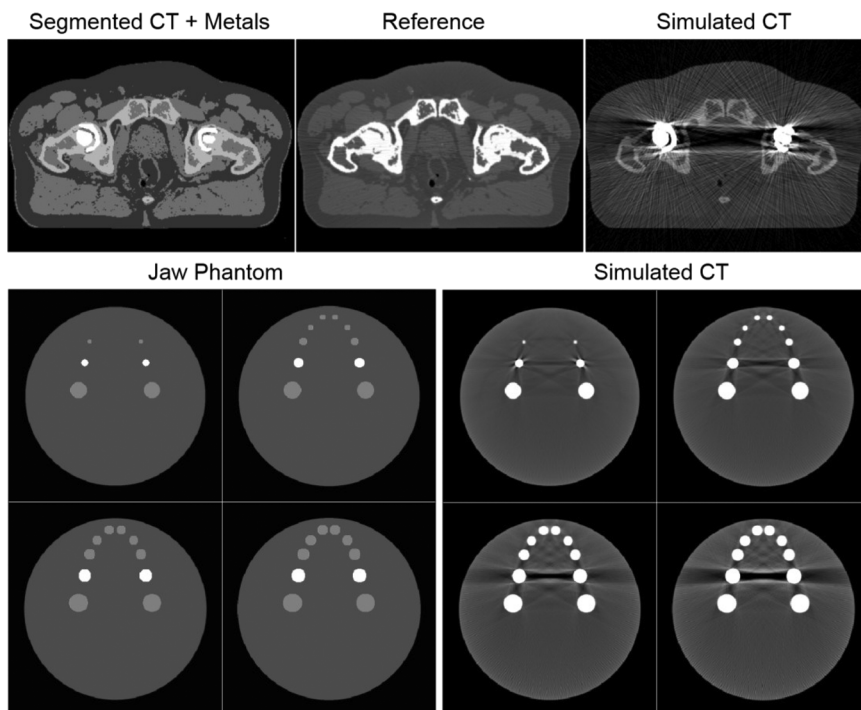


Fig. 3. Simulation of metal artifacts in a 2D bi-lateral hip prostheses phantom (top panel) and a 3D jaw phantom (bottom panel) based on the polychromatic propagation of X-ray beams. In the hip phantom, an original CT image was segmented into bone, soft and normal tissues. A polychromatic data acquisition was performed on the segmented image to obtain an artifact-free reference image. To simulate metal artifacts, two metallic implants were superimposed on the segmented CT image and the transmission data were acquired using a polychromatic X-ray CT transmission model considering the scattering due to metallic implants. The jaw phantom was designed for 3D cone-beam CT and consists of several spheroids representing teeth and two simulated dental fillings within a large spheroidal soft tissue region. In this phantom, the metal artifacts were also simulated by considering a polychromatic CT model.

falls below a tolerance ( $\eta = 1 \times 10^{-4}$ ). In this work, we set  $\delta = 5 \times 10^{-4}$  and  $\alpha = 0.95$  in (6) for all the datasets presented in the Results section.

### C. Prior and Metal-Only Images

To obtain a tissue-classified prior image from CT images with streaking dark and bright artifacts, Bal and Spies [8] applied 2D filtering to uncorrected CT images, tailored to reduce noise and streaking artifacts, and classified them into air, soft tissue, normal tissue, bone, and metal regions using K-means clustering. An average CT number was then assigned to each region. In this work, we segmented the uncorrected CT images into air, bone, soft tissue and lung (if present in the field-of-view) using a simple thresholding technique [26], [45]. Following tissue classification, CT numbers of air and soft tissue regions were set to  $-1000$  and  $0$  HU, respectively, and the numbers of bone as well as lung regions were kept the same as the original image because of the inherent variability of bone and lung tissue densities and as such the corresponding CT numbers. In the segmentation of uncorrected CT images into different tissues, severe dark and bright streaking artifacts can be falsely classified as air and bone in the segmented soft tissue and bone images, respectively. Following the work of Karimi *et al.* [53] on the derivation of a prior image, we applied a 3D close and open morphological filtering on the segmented classes to reduce these errors. In cases with severe artifacts, the residual misclassifications were interactively reduced using a graphical user interface. As suggested by Prell *et al.* [45], an alternative way would be to segment an image pre-corrected using a linear interpolation MAR algorithm. However, in some cases, we noticed that linear interpolation and

its improved 3D triangulated version fail to effectively reduce streaking artifacts. The segmentation of metallic implants and thus generation of a metal-only image was performed by simple thresholding at about 3000 HU for dental fillings and 2000 HU for other implants. In the obtained prior image, we assigned the CT number of soft tissue to the segmented metal implants. Following the generation of prior and metal-only images, a prior sinogram as well as metal traces (missing projections) were obtained by line-integral forward projections.

### D. Simulation and Clinical Studies

The performance of the proposed MAR algorithm was compared with 3D linear interpolation (LI) implemented on a Delaunay triangulated grid and the normalized metal artifact reduction (NMAR) algorithms using simulated and clinical studies. To objectively evaluate the performance of algorithms with respect to a reference CT image (i.e. without metal artifacts), we retrospectively generated metal artifacts in artifact-free images of two simulated phantoms i) a patient with bilateral hip prostheses and ii) a jaw phantom with dental fillings. These phantoms were designed to evaluate the performance of the algorithm for both 2D fan-beam and 3D cone-beam geometries, respectively. As shown in Fig. 3, the hip phantom was constructed by segmenting an original CT image into 3 classes, i.e. air, soft tissue and bone plus iron prostheses. The jaw phantom was analytically modeled from several spheroids, simulating teeth with radii ranging from 8 to 20 mm, and a large sphere simulating the head. For this phantom, we considered two dental fillings.

To simulate beam hardening and the resulting streaking artifacts, we modeled the polychromatic propagation of X-ray

TABLE I  
SUMMARY OF CT SCANNING PARAMETERS USED IN THE CLINICAL STUDIES

	Hip prostheses	ECG electrodes	Dental fillings	Spine fixation	Hip prosthesis
Tube voltage (kVp)	100/120	140/120	120	120	120
Tube current (mA)	40/32	179/175	166/116	95	99
Exposure time (ms)	500	1500/1000	750/500	500	500
Slice thickness (mm)	2	3	5	5	2

beams for the bilateral hip and jaw phantoms, according to the following model [54]:

$$\mathbf{g}_i = \sum_{k=1}^K \text{Poisson} \left\{ I_k^{(i)} \exp \left[ - \int_{\mathcal{L}_i} \mu(\mathbf{l}, E_k) dl \right] + S_k^{(i)} \right\} \quad (11)$$

where  $\mathbf{g}_i$  is the measured number of photons in projection bin  $i$ ,  $I_k^{(i)}$  is the number of incident photons at  $k$ th energy along projection line  $i$ ,  $\mu(\mathbf{l}, E_k)$  is the energy-dependent attenuation map for different tissue classes and  $S_k^{(i)}$  accounts for the contribution of scatters. A polyenergetic X-ray spectrum was generated using SpekCal software [55] for a tube voltage of 120 kVp, 2.5 mm aluminum filtration, 10 degrees anode angle and a tube output of 123.8  $\mu\text{Gy/mAs}$  at 1 meter. The spectrum was uniformly sampled for  $K = 35$  monoenergetic X-ray beams with an intensity and average energy calculated over each energy interval. For each tissue class, energy-dependent linear attenuation coefficients were derived and interpolated from the NIST XCOM photon cross section library [56]. The attenuation maps were forward projected and then according to (11), the Poisson noise realization of the transmission and scatter sinograms were summed up to get a sinogram acquired under the conditions of polychromatic propagation of X-ray beams. In this work, we considered a constant-level scatter for non-zero projection bins [57]. The resulting sinogram was log-processed and reconstructed by FBP and FDK algorithms. As shown in Fig. 3, the reconstructed artificial CT images suffer from beam hardening and streaking artifacts in a similar way as in real CT acquisitions. In our simulations, non-linear partial volume effect was not modeled. Following the generation of an artificially degraded image, we obtained a prior image, metallic implants, missing projections in the sinograms resulting from the polychromatic propagation of X-ray beams. In addition, for each dataset a reference image was obtained using the above-mentioned procedure by considering the metallic implants as bony structures and ignoring scatter. For metal artifact reduction in the hip phantom and clinical datasets, we evaluated the performance of the proposed algorithm using artificial sinograms obtained from the fan-beam forward projection of uncorrected CT images.

To acquire artificial projection data under conditions closely matching actual acquisition, we considered the fan-beam geometry of a simulated single-slice CT scanner with 888 detector channels, 984 angular samples over a 360 orbit, detector pitch of 1 mm, 949 mm source to detector distance, 541 mm source to iso-center distance, 408 mm iso-center to detector distance. The geometric system matrix describing this scanner was generated by the Image Reconstruction Toolbox (IRT) [58], running in MATLAB 2010a (The MathWorks, Inc., Natick, MA) on a

12-core workstation with 2.4 GHz Intel Xeon processors and 32 GB memory.

Line integrals were employed during forward projection to obtain the Radon transform. For the evaluation of the algorithm for the jaw phantom, we simulated a cone-beam flat-panel CT scanner with the following specifications: a flat panel detector with a matrix size of  $384 \times 320$  and crystal size of  $1.56 \times 1.56 \text{ mm}^2$ , 800 mm source to iso-center distance, 470 mm iso-center to detector distance and 360 projection angles. The  $384 \times 320 \times 360$  projection dataset of the jaw phantom was obtained using the IRT toolbox. Following the correction of the sinograms of the hip phantom and clinical studies, the corrected images were reconstructed using the FBP algorithm with Ram-Lak filter, for a resolution of  $512 \times 512$  with pixel size of 0.97 mm and a 500-mm field-of-view. The Ram-Lak filter was chosen to best preserve the sharpness of the reconstructed images. The corrected images of the jaw phantom were reconstructed using the FDK algorithm with a matrix size of  $512 \times 512 \times 20$  and voxel size of  $1 \times 1 \times 2 \text{ mm}^2$ . For the clinical evaluation of the MAR algorithm, CT datasets of 8 patients were used. The data were acquired in helical mode on the Biograph 64 True Point PET/CT and Sensation 16 CT scanners (Siemens Healthcare, Erlangen, Germany), equipped with 40- and 24-row detectors, respectively. The datasets include uni- and bi-lateral hip prostheses, dental fillings, EEG electrodes, shoulder prosthesis and spine fixation with pedicle screws. Table I summarizes CT scanning parameters of the datasets.

### E. Evaluation Metrics

The performance of the proposed algorithm was subjectively and objectively compared with 3D linear interpolation and NMAR algorithms. In simulation studies, the performance of the algorithms in terms of reducing streaking artifacts was objectively evaluated with respect to a reference using region of interest (ROI) analysis. For this purpose, two ROIs were drawn on uncorrected images and the normalized root mean square difference (NRMSD) and mean absolute deviation (MAD) between corrected images ( $\mathbf{f}^{MAR}$ ) and their reference image ( $\mathbf{f}^{Ref}$ ) were calculated for each ROI as follows:

$$\text{NRMSD}(\%) = 100 \times \sqrt{\frac{\sum_{i \in \text{ROI}} (\mathbf{f}_i^{MAR} - \mathbf{f}_i^{Ref})^2}{\sum_{i \in \text{ROI}} (\mathbf{f}_i^{Ref})^2}} \quad (12)$$

$$\text{MAD}(\text{HU}) = \frac{1}{N} \sum_{i \in \text{ROI}} |\mathbf{f}_i^{MAR} - \mathbf{f}_i^{Ref}| \quad (13)$$

For quantitative evaluation of the MAR algorithms for the clinical datasets, we calculated mean and standard deviation of CT numbers in volumes of interests (VOI) defined on uncorrected

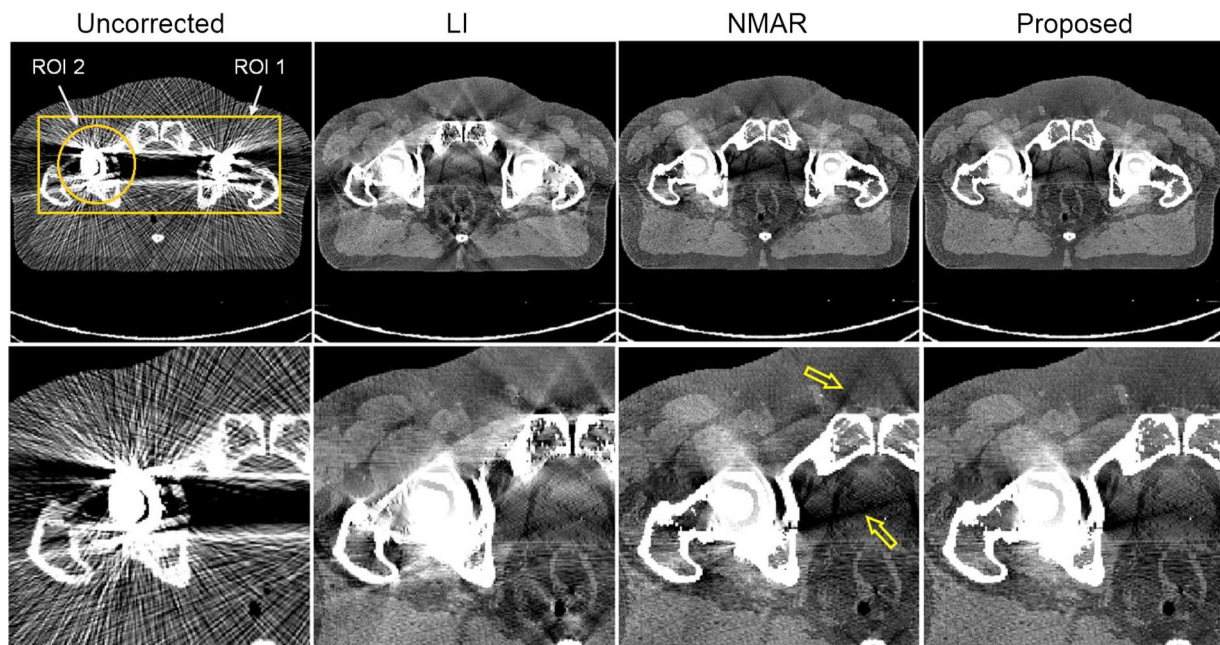


Fig. 4. Comparison between the proposed and other MAR algorithms for the simulated bi-lateral hip prostheses dataset (WW/WL = 450/50 HU).

TABLE II  
QUANTITATIVE EVALUATION OF THE MAR ALGORITHMS FOR THE SIMULATED HIP AND JAW PHANTOMS IN TERMS OF NORMALIZED ROOT MEAN SQUARE DIFFERENCE (NRMSD) AND MEAN ABSOLUTE DEVIATION (MAD) METRICS

Phantom	ROI/VOI	Uncorrected		LI		NMAR		Proposed	
		NRMSE (%)	MAD (HU)	NRMSE (%)	MAD (HU)	NRMSE (%)	MAD (HU)	NRMSE (%)	MAD (HU)
Hip	1	69.20	92.76	20.02	42.47	20.56	41.37	18.62	40.30
	2	118.29	190.29	19.76	65.53	21.29	68.39	19.55	64.95
Jaw	1	18.28	18.69	5.95	18.59	3.40	7.81	3.23	4.64
	2	8.72	28.56	1.35	4.66	1.13	4.62	0.60	2.50

and corrected CT images over streaking artifacts. Owing to the absence of a reference artifact-free image in the clinical datasets, we defined a reference VOI on uncorrected images far from streaking artifacts.

### III. RESULTS

#### A. Simulation Studies

Fig. 4 compares the performance of MAR algorithms for the simulated bilateral hip study. In this dataset, the algorithms have noticeably reduced streaking artifacts. However, the visual comparison reveals that the proposed algorithm results in the production of less new artifacts as pointed by the arrows. It should be noted that both NMAR and the proposed algorithm depict a similar dark streak over the bladder because both use the same prior image. However, the proposed algorithm shows noticeable reduction of this artifact. For the objective comparison of the algorithms with respect to the reference image shown in Fig. 3, two ROIs were defined on the uncorrected CT image (see Fig. 4): one large rectangular ROI, namely ROI 1, to capture a large affected area, and one circular ROI, namely ROI 2, for local evaluation near the implants. Table II summarizes the NRMSD and MAD results.

In the ROI-based evaluations, the regions of metallic implants were excluded from the ROIs of (un-)corrected and reference

images, since the implants are finally added back to the corrected images. The results show that the proposed algorithm achieves a better local and global performance, which is consistent with the subjective evaluation.

Fig. 5 compares the performance of MAR algorithms for the cone-beam CT study. The figure also shows the simulated reference and uncorrected images. As mentioned in Section II-D, in the reference image, the metallic implants were replaced by bones and the projection data were analytically acquired using the polychromatic X-ray propagation model defined in (11). As can be seen, the reference reconstructed images suffer from streaking artifacts between teeth and an overall cupping artifact due to beam hardening effect and the incapability of the FDK algorithm in considering the non-linear and selective absorption of the X-ray photons. The subjective comparison of the corrected images demonstrates that, contrary to 3D linear interpolation and NMAR, the proposed 3D MAR algorithm has remarkably reduced metallic artifacts without introducing new artifacts. Note that the images were only corrected for metal artifacts and as such, beam hardening artifacts between teeth are still present. In this dataset, we performed the interpolation step of the NMAR algorithm on sinogram views of the 3D projections of the jaw phantom. A volumetric prior image was constructed by replacing the metallic implants of the jaw phantom with soft tissue and its corresponding projection obtained using

TABLE III  
 QUANTITATIVE EVALUATION OF THE STUDIED MAR ALGORITHMS FOR THE CLINICAL DATASETS, SHOWN ON THE TOP (T) AND BOTTOM (B) PANELS OF FIGS. 6–9, IN TERMS OF MEAN AND STANDARD DEVIATION OF CT NUMBERS WITHIN A VOLUME OF INTEREST DRAWN ON ARTIFACTUAL REGIONS (SEE THE FIGURES) AND ON A BACKGROUND REFERENCE REGION FAR AWAY FROM THE ARTIFACTS

Dataset (Figure)	Panel	Background	Uncorrected	LI	NMAR	Proposed
Hip prostheses (6)	T	$36.0 \pm 39.0$	$-53.5 \pm 209.0$	$30.26 \pm 181.4$	$72.0 \pm 150.8$	$39.4 \pm 171.2$
	B	$0.78 \pm 36.8$	$-184.1 \pm 272.2$	$-114.0 \pm 190.4$	$-14.0 \pm 185.9$	$-34.39 \pm 189.0$
EEG electrodes (7)	T	$32.6 \pm 12.9$	$38.7 \pm 25.4$	$36.9 \pm 17.1$	$45.3 \pm 14.2$	$33.9 \pm 13.4$
	B	$36.4 \pm 30.8$	$48.4 \pm 134.5$	$44.7 \pm 124.6$	$43.2 \pm 120.8$	$40.2 \pm 119.9$
Dental filling (8)	T	$20.8 \pm 19.2$	$34.7 \pm 74.7$	$34.5 \pm 69.2$	$66.0 \pm 40.3$	$23.0 \pm 38.2$
	B	$21.2 \pm 25.3$	$64.3 \pm 235.6$	$108.3 \pm 102.6$	$111.2 \pm 105.3$	$75.8 \pm 91.3$
Shoulder prosthesis (9)	T	$0.8 \pm 44.2$	$-94.1 \pm 145.7$	$-30.4 \pm 82.2$	$-8.0 \pm 75.2$	$-10.85 \pm 88.0$
Spin fixation (9)	B	$29.6 \pm 18.8$	$-83.7 \pm 154.5$	$-43.2 \pm 106.8$	$-41.9 \pm 102.1$	$-52.7 \pm 105.7$

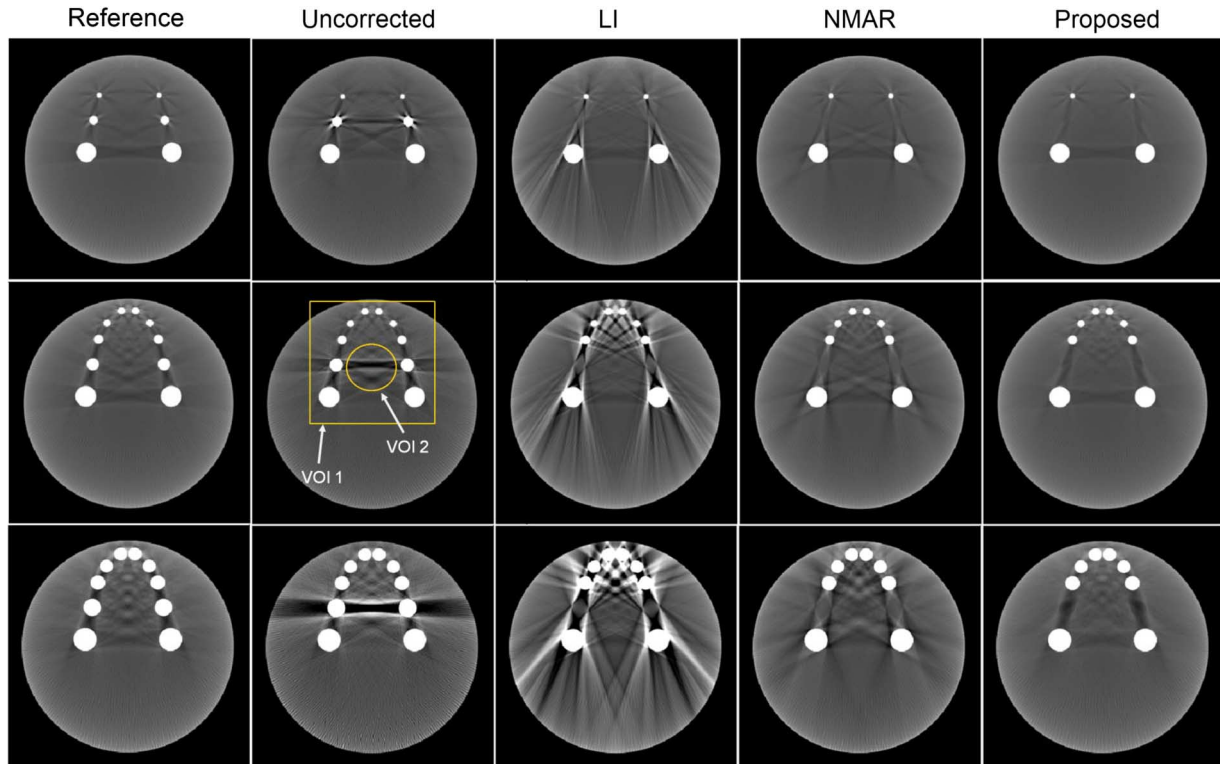


Fig. 5. Comparison between the proposed and other MAR algorithms for the jaw phantom simulated for 3D cone-beam CT imaging (The display window is the same for all images).

a monochromatic X-ray model at 80 kVp. The same prior sinogram was then employed for both NMAR and the proposed algorithm. As shown in Fig. 5, two VOIs were defined on the uncorrected images and the NRMSE and MAD metrics calculated. The results presented in Table II show that the proposed algorithm also outperforms its counterparts when using objective metrics.

### B. Clinical Studies

Fig. 6 compares the performance of MAR algorithms for the clinical hip studies with uni- and bi-lateral prostheses. As summarized in Table I, the patients have undergone a low-dose CT scan for PET attenuation correction and therefore metallic implants have resulted in severe dark and noisy streaking artifacts mainly due to beam hardening and photon starvation. In the uni-lateral hip prosthesis dataset, the studied algorithms have noticeably reduced the artifacts; however, LI and NMAR algorithms have introduced new artifacts (follow the arrows). As can be seen, the NMAR algorithm has particularly introduced flare

at the borders and around the prosthesis, which should be attributed to the propagation of interpolation errors during (de-)normalization. While the proposed algorithm has effectively reduced the artifacts, it has obscured the details of the hip prosthesis in the axial direction (see sagittal view). This is due to the fact that the projection data of the studied clinical studies were obtained by stacking the 2D sinograms of a sequence of CT slices, which might not be fully correlated in the third dimension as in cone-beam CT. Hence, the proposed MAR algorithm shows slightly axial detail degradation in the displayed window setting.

For objective assessment of the algorithms, a VOI was drawn on the area suffering from dark artifacts, as shown in the coronal slice. Note that in this and the following figures, we only show VOIs in one dimension. A background VOI was also defined on a region far away from the artifacts. The mean and standard deviation of CT numbers of the reconstructed image over the VOIs are summarized in Table III. The results show that the proposed algorithm gives rise to a closer mean value to the background

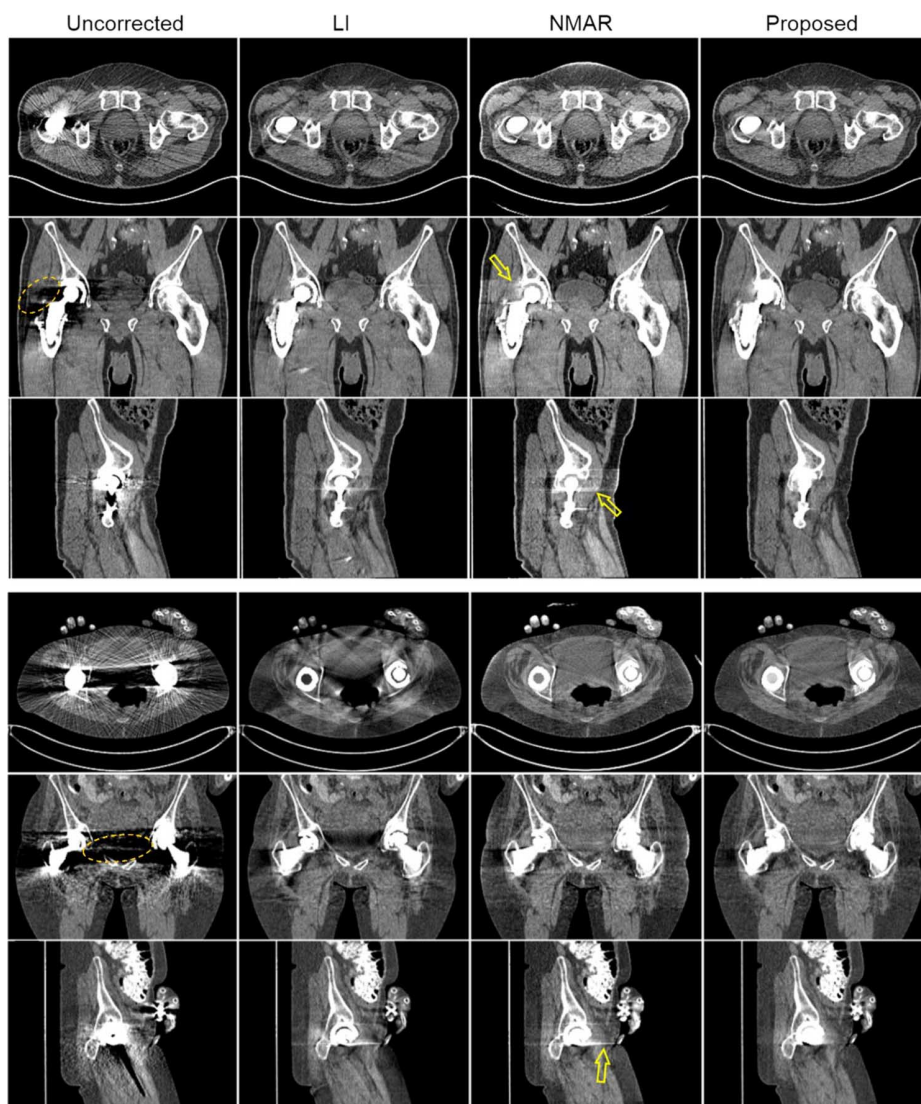


Fig. 6. Comparison between the proposed and other MAR algorithms for the clinical uni- and bi-lateral hip prostheses datasets (WW/WL = 500/50 HU).

mean value, while NMAR shows a noticeable difference with respect to background. In the bi-lateral hip prostheses dataset (shown in Fig. 6 bottom panel), both NMAR and the proposed algorithm have substantially reduced the artifacts, while linear interpolation has introduced new artifacts. The subjective evaluation of corrected images shows that the proposed algorithm has reduced the artifacts without introducing bright streaks emanating from the prosthesis (see arrow). The VOI analysis (Table III), however shows that NMAR has more effectively reduced the dark streaks between the hips (over the region shown in Fig. 6 on the coronal slice). The sizes of the projection data of these datasets were  $888 \times 984 \times 103$  and  $\times 99$ . In the recovery of missing projections, the proposed algorithm converged, on average, after 95 iterations with elapsed computation time of 657 seconds. In order to reduce computation time, we trimmed the radial bins of the projection data to those passing through the patient body. This procedure reduces the matrix size of projection datasets and therefore reduces the number of arithmetic operations during the calculation of 3D finite differences.

Fig. 7 compares the performance of MAR algorithms for two patients with EEG electrodes. As can be seen in these datasets,

the proposed algorithm has more effectively reduced the artifacts in comparison with LI and NMAR algorithms. In these datasets for which the metallic implants are outside the skull, we noticed that the NMAR algorithm introduces wide and severe bright and dark streaking artifacts at the borders near the electrodes, which are due to the normalization of projection bins by small values at these regions. To practically reduce this effect, we expanded the soft tissue region of prior images for this algorithm and also thresholded the very high-valued projections of de-normalized sinograms to a normal value. Furthermore, to avoid division by zero during normalization, we set zero bins in the sinogram of the prior image to 1. Small threshold values have been suggested by Meyer *et al.* [26]; however, these values can result in highly inaccurate values in the normalized sinograms and hence can contribute to the appearance of severe bright streaking artifacts in the EEG datasets.

As indicated by the arrows in Fig. 7, the improved NMAR still give rise to new artifacts, particularly in the bottom dataset which has more electrodes. The reduced streaks artifacts in the regions close to the electrodes is of importance in CT-based attenuation correction of PET data, specifically in patients with

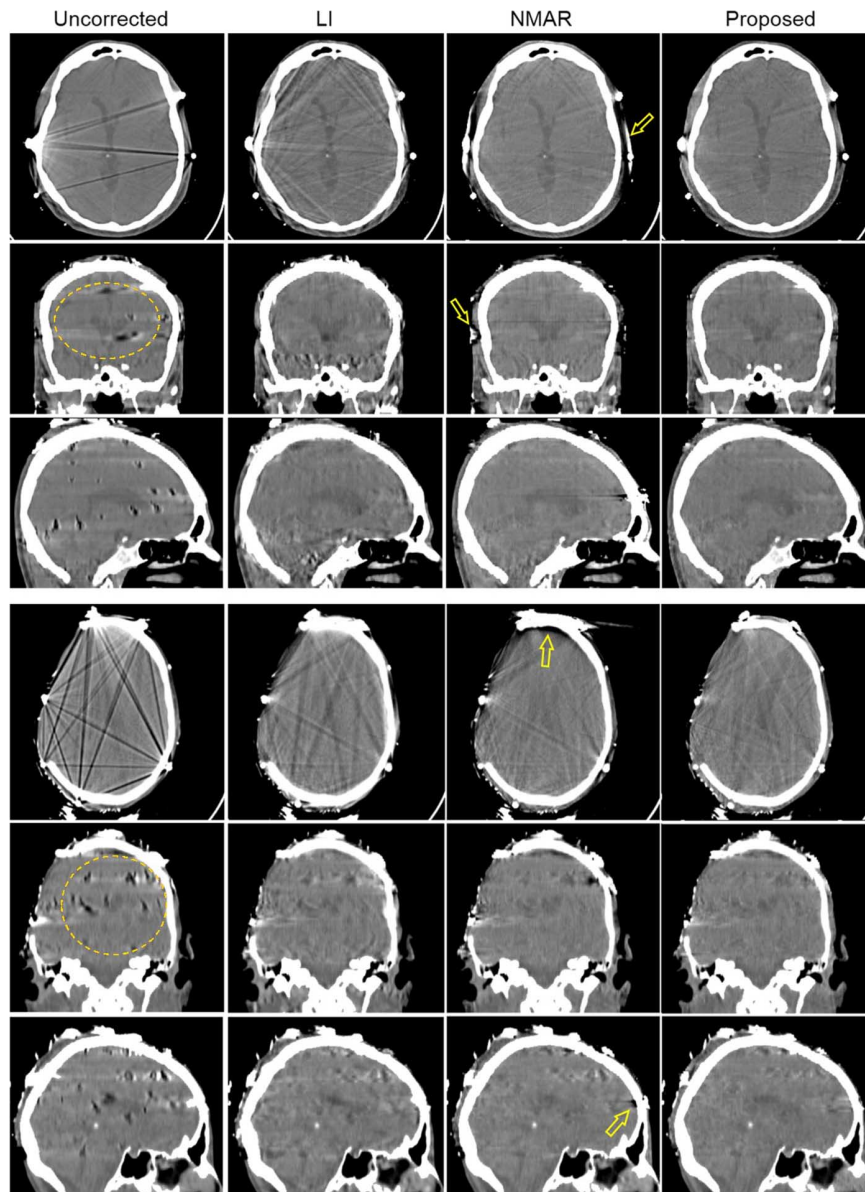


Fig. 7. Comparison between the proposed and other MAR algorithms for the clinical head EEG datasets ( $WW/WL = 350/50$  HU).

epileptic foci [59]. For quantitative evaluation of the algorithms, two large VOI were defined in the cranium covering most of the streaks, as shown in Fig. 7. The results for both datasets (Table III) demonstrate that the proposed algorithm depicts an improved performance over LI and NMAR algorithms by achieving a mean CT number close to the background VOI. These datasets had 82 and 83 slices and the proposed algorithm converged, on average, after 194 iterations within 776 seconds. Fig. 8 compares the performance of MAR algorithms for two clinical head datasets with multiple dental fillings. The reduction of metallic artifacts arising from multiple dental fillings is somewhat a challenging task, since their metal traces in the sinogram domain are usually unified in some angles and result in a large missing region. As can be seen in both datasets, linear interpolation has introduced dark streaking artifacts, while NMAR and the proposed algorithm have more effectively reduced the artifacts. As mentioned earlier, these two algorithms exploit some prior information for the interpolation of missing

projections. However, the images shown in Fig. 8 show that the NMAR algorithm depicts a flare in the lip region of the top dataset and in the palatine region of the bottom dataset (see arrows). Conversely, the proposed algorithm, which uses the same image prior, does not result in such new artifacts, which should be ascribed to error propagation during de-normalization.

As shown in the sagittal slices shown in Fig. 8, two VOIs were defined in the oral cavity for objective comparison of the algorithms. Consistent with the subjective observations, the results in Table III show that the NMAR algorithm overestimates CT numbers in comparison with the background VOI. The results also confirm the outperformance of the proposed algorithm in the oral cavity region. These datasets had 13 and 16 slices and the proposed algorithm has converged, on average, after 169 iterations within 129 seconds.

Fig. 9 (top panel) compares the performance of MAR algorithms for a clinical study with unilateral shoulder prosthesis.

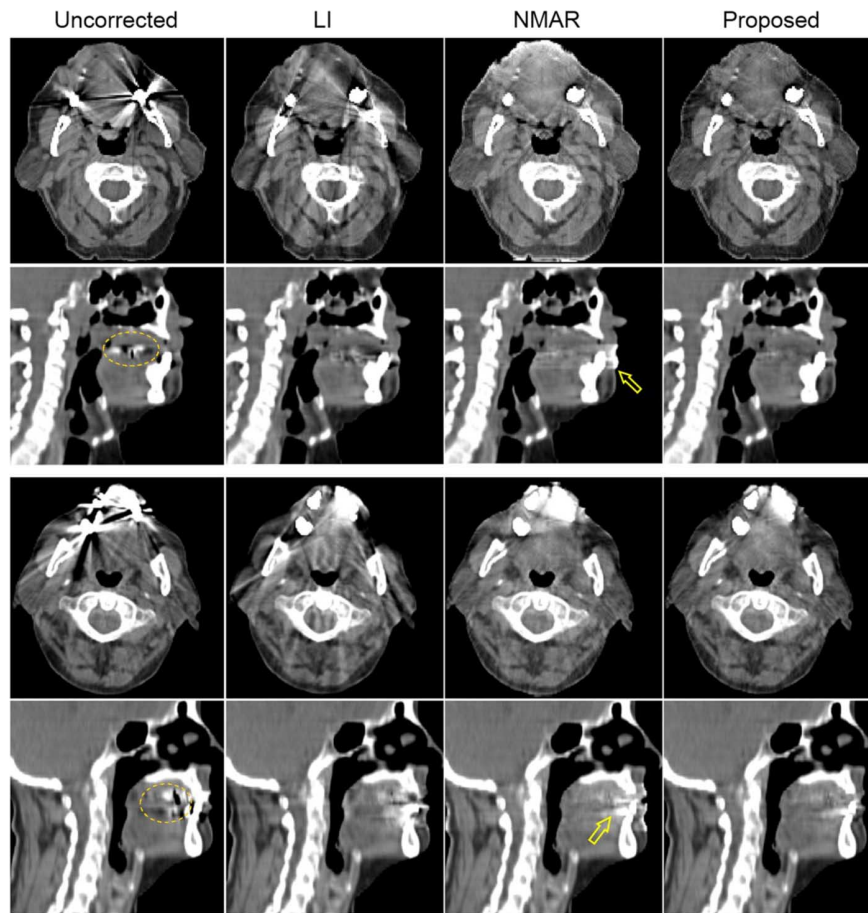


Fig. 8. Comparison between the proposed and other MAR algorithms for the clinical dental filling datasets ( $WW/WL = 500/50$  HU).

The uncorrected images suffer from severe dark streaks radiating from the implant. The results show that the algorithms have substantially reduced the dark streaking artifacts; however, LI has introduced new bright artifacts while NMAR depicts some residual bright artifacts (see arrows). The performance of the proposed algorithm is comparable with NMAR but with reduced bright artifacts. For quantitative comparison of the different MAR algorithms, a VOI was drawn over regions affected by dark streaks (as shown in the transverse slice) and the mean and standard deviation of CT numbers were calculated. The results shown in Table III portray that NMAR and the proposed algorithms achieve comparable performance in terms of artifacts reduction in the selected volume of interest. Fig. 9 (bottom panel) compares the performance of MAR algorithms for a clinical study with spine fixation. For this challenging case where the metallic implants are located close together and surrounded by several bony structures, linear interpolation has limited performance. This makes the pure interpolation of missing projections from adjacent projections inefficient and even inaccurate. As can be seen, both NMAR and the proposed algorithm have substantially reduced the dark streak artifacts; however, as can be observed in the sagittal views, the residual dark artifacts in the image corrected using the proposed algorithm are more pronounced in front of the vertebrae in comparison with LI and NMAR. At the same time, as shown by the black arrow, the proposed algorithm shows less artifacts in the rear of the vertebrae. The

quantitative performance of the algorithms in reducing the dark artifacts in the VOI shown on the sagittal slice reveals that.

In this region, LI and NMAR perform better. In these datasets, the number of slices were 99 and 101 and the proposed algorithm converged, on average, after 195 iterations within 996 seconds.

Fig. 10 compares the performance of the evaluated algorithms in the projection domain. The top panel shows the zoomed-in scout and sinogram views of the bilateral hip dataset shown in Fig. 6. Similarly, the bottom panel compares the same views of the EEG head dataset shown in Fig. 7 (top panel). As can be seen, the LI algorithm, implemented in a 3D triangulated grid, cannot effectively interpolate the missing projections, particularly in the case of hip prostheses where a large number of projections have been corrupted and the neighboring projections are not so much informative. The comparisons between NMAR and our algorithm for the hip dataset show that both algorithms have similar performance; however, as shown by the arrow, NMAR is susceptible to the propagation of error during linear interpolation which simply bridges the missing projections in the radial direction. The comparison of these algorithms for the EEG dataset shows that the proposed algorithms restore the missing projections more accurately than NMAR. As pointed by the arrow, the NMAR algorithm results in high-value false projections near the electrodes, which are due to erroneous normalization. As mentioned earlier, we substantially reduced

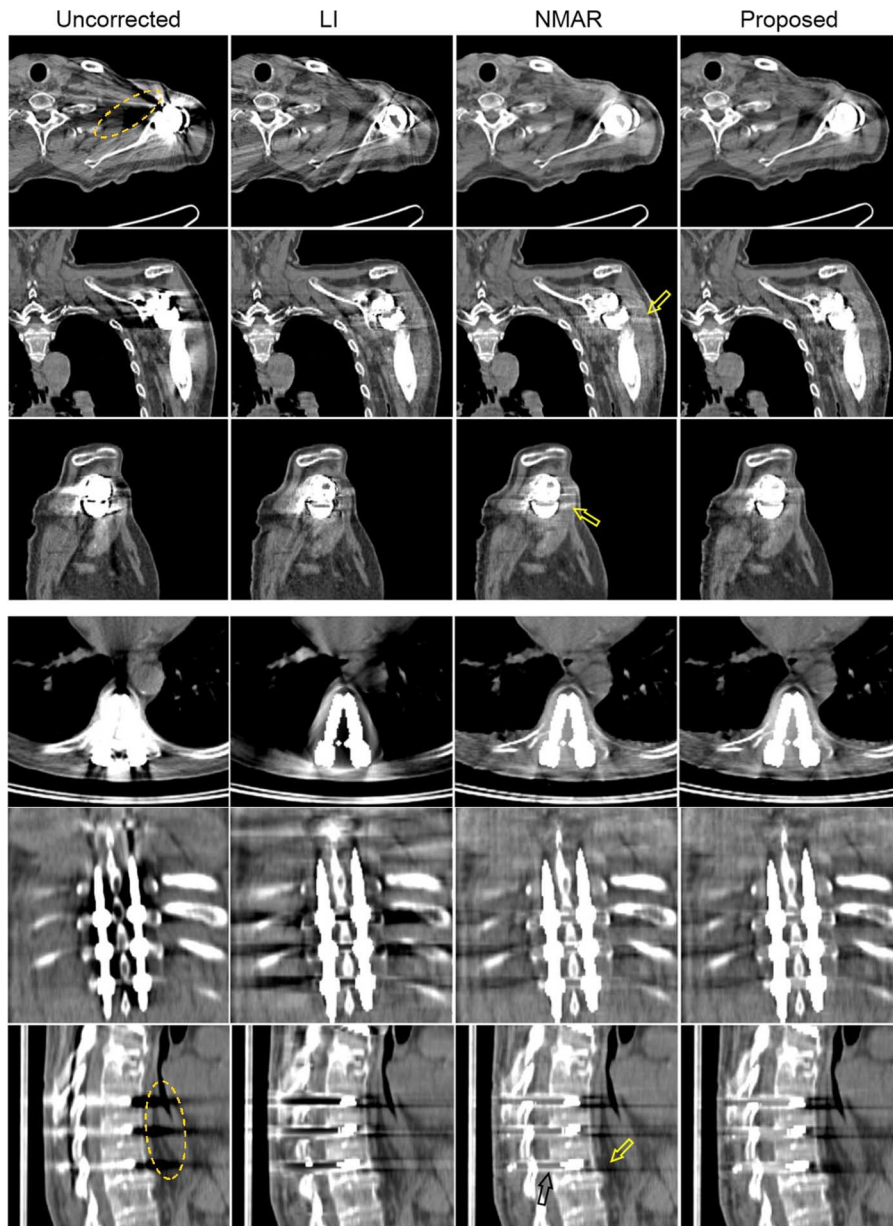


Fig. 9 Comparison between the proposed and other MAR algorithms for the clinical shoulder and spine datasets (WW/WL = 500/50 HU).

these errors by expanding the soft tissue component of the prior image. The inspection of the sinogram views also show that the proposed algorithm more accurately and smoothly restores the missing projections compared to its counterparts.

#### IV. DISCUSSION

Streaking artifacts arising from metallic implants can degrade the quality of CT images and impact the clinical relevance of this diagnostic procedure by obscuring the radiological manifestation of tissues surrounding the implants. In this work, we introduce a 3D MAR algorithm for reducing metal artifacts in a fan-beam and cone-beam CT scanners. In this algorithm, the recovery and completion of missing projections was formulated as a maximum *a posteriori* (MAP) estimation, in which our expectations and prior knowledge about the missing projections

was imposed using a novel prior potential function. This function was developed to interpolate the missing projections from available projection data and at the same time, to exploit prior projection (sinogram) data obtained from the forward projection of a tissue-classified CT image. As elaborated in Section II. A, we exploit the compressibility of a residual sinogram, obtained from the subtraction of the target (unknown) and prior sinograms, as a prior knowledge. The compressibility or sparsity of the residual sinogram is further promoted using discrete gradients, which is known as a sparsifying transform, and a modified Perona-Malik diffusivity function defined on the prior sinogram. We compared the performance of the proposed algorithm with two popular and state-of-the-art MAR algorithms, namely a 3D linear interpolation implemented on an irregular grid and Meyer's NMAR algorithm using simulation and clinical studies. Based on subjective and objective evaluations, it

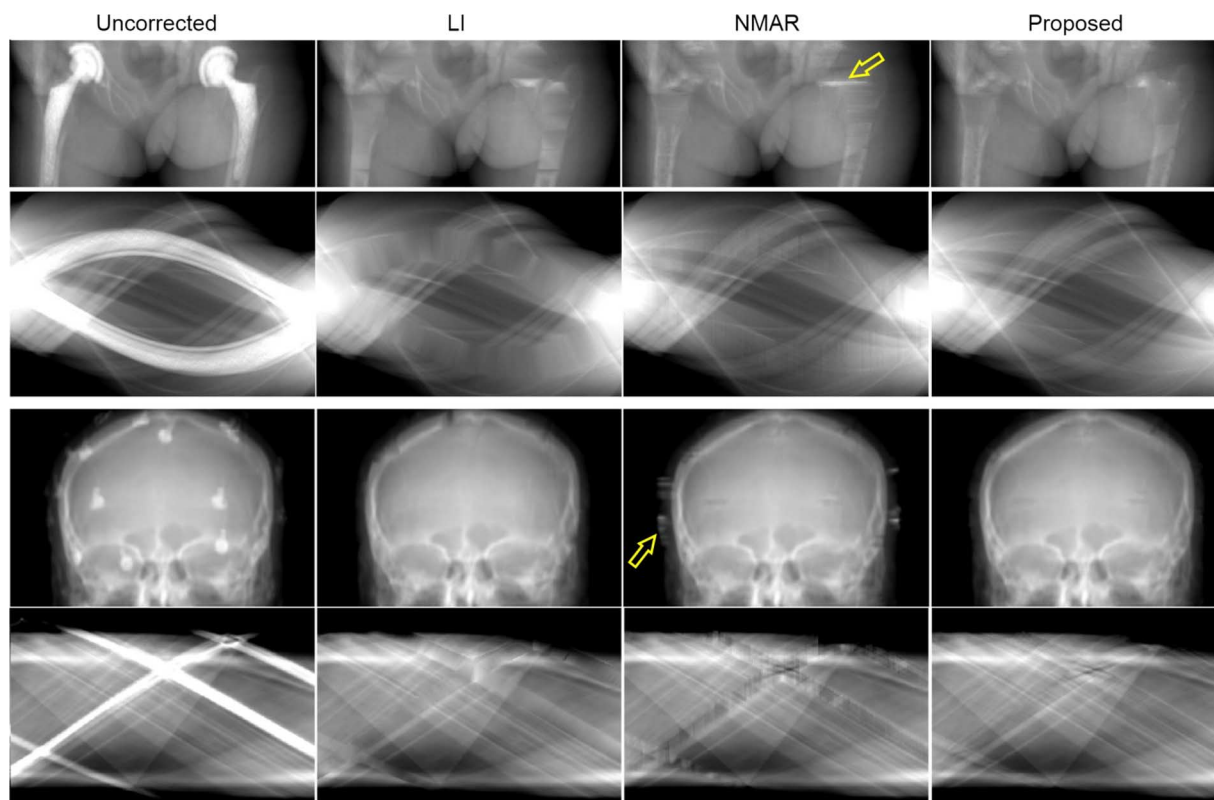


Fig. 10. Comparison of the scout scans and sinogram views of projection data completed by the studied MAR algorithms. Top to bottom panels: Projection data of the bi-lateral hip prosthesis study (shown in Fig. 6, top panel) and the data of the EEG electrode study (shown in Fig. 7, top panel). As indicated by the arrows, the proposed algorithm is not susceptible to interpolation and normalization errors of LI and NMAR algorithms.

was found that the proposed algorithm can generally outperform its counterparts for both 2D fan-beam and 3D cone-beam CT imaging. In the implementation of NMAR and the proposed algorithm, we used the same prior image obtained by the procedure described in Section II-C. As demonstrated in our results, the proposed algorithm is not susceptible to interpolation and normalization errors encountered in the NMAR algorithm, particularly when metallic implants are at the surface of the body as in epileptic patients presenting with EEG electrodes. However, both algorithms are susceptible to segmentation errors of the prior image. These errors are mostly due to the classification of dark streak artifacts as air within the soft tissue component of the prior image. As shown in [8], these errors can reappear in the reconstructed images. Recently, several studies focused on accurate segmentation of different tissues from metal artifacts in uncorrected CT images. Chen *et al.* [60] used non-local filtering and mutual information maximized segmentation to improve the performance of Bal and Spies' method [8] for the classification of biological tissues. Karimi *et al.* [53] proposed to apply close and open morphological operations on uncorrected images in order to reduce dark and bright artifacts. This procedure is then followed by a region growing segmentation guided by a distance-dependent threshold that limits the grouping of artifacts as anatomy. However, these approaches might fail in cases with large or multiple closely-seated implants [53]. To more practically reduce segmentation errors, Prell *et al.* [45] suggested tissue classification on a CT image corrected by linear interpolation. This idea has recently motivated some recent at-

tempts to iteratively improve the derivation of the prior image [61], [62]. There are also other approaches enabling to avoid segmentation errors and possibly to improve the accuracy of recovered projections by defining a prior image from statistical anatomical atlases [63].

In the proposed prior function defined in (6), we introduced a relaxation parameter  $\alpha$  which can be used to control the impact of the prior image in the recovery of missing projections. In cases with severe segmentation errors in the prior image, this parameter can be set to a small value or zero, thereby the errors are reduced or eliminated in the reconstructed image. However, as mentioned earlier, as  $\alpha$  decreases to zero, the proposed prior reduces to a Tikhonov quadratic prior. Therefore, the performance of the algorithm degrades to that of conventional MAR algorithms. The Perona-Malik diffusivity function defined in (6) includes the contrast parameter  $\delta$ , which controls the amount of edge-enhancement. Since CT projection data are usually smooth, we set  $\delta = 5 \times 10^{-4}$  in this work for all used datasets and found that this value is fairly small in order to guide the completion of missing projections. Generally, smaller values of  $\delta$  have a negative impact on the convergence of the employed projected gradient algorithm. Nevertheless, we improved the convergence rate and thus the computation time of the optimization algorithm using Nesterov's acceleration, as formulated in Algorithm 1. In terms of computation time, our results show that the 3D linear interpolation on a triangulated mesh and NMAR are the most time-consuming and fastest MAR algorithms, respectively. In a dataset having size of  $888 \times 984 \times 103$ , the

elapsed computation times are about 1630 and 25 seconds, respectively, on our MATLAB-based implementations. Note that since the 3D LI algorithm is memory demanding for such a dataset, it was implemented for every 10 slices. For the clinical studies used in this work, the performance of the various MAR algorithms was evaluated using artificial projection data obtained from the forward projection of uncorrected images, whereas for simulation studies, the algorithms were evaluated on the original projection data. Joemai *et al.* reported that the correction of corrupted projections on original scanner-specific raw data is more effective than corrections performed on artificial data [64]. However, we followed the latter generic method for the clinical studies while considering the geometry of a realistic fan-beam CT scanner and put more emphasis on the development of a new MAR algorithm that reduces metal artifacts as efficiently as or better than current state-of-the-art MAR algorithms.

## V. CONCLUSION

In this study, a 3D MAR algorithm was proposed in the maximum *a posteriori* completion of missing projections in a sequence of 2D CT slices and 3D cone-beam CT. In this algorithm, we exploited side information about missing projections, obtained from a tissue-classified prior CT image using a novel prior potential function. The prior was designed to exploit and promote the sparsity of a residual projection dataset (sinogram) obtained from the subtraction of the unknown target dataset from the projection dataset of the tissue-classified prior image. The formulated MAP problem was casted as a constrained optimization problem and solved using an accelerated projected gradient algorithm. The proposed algorithm was compared with two state-of-the-art algorithms using simulation and clinical studies. In 2D fan-beam and 3D cone-beam simulations, it was demonstrated that the proposed 3D algorithm outperforms its counterparts, particularly in cone-beam CT. In the clinical studies, the performance of the evaluated MAR algorithms was evaluated using artificial sinograms of a sequence of 2D CT slices. It was found that the proposed algorithm effectively reduces metal artifacts without introducing new ones owing to more accurate utilization of prior information in comparison with its state-of-the-art counterparts. Future work will focus on the application of the proposed MAR algorithm in clinical 3D cone beam CT imaging.

## ACKNOWLEDGMENT

This work was supported by the Swiss National Science Foundation under grant SNSF 31003A-135576, the Indo-Swiss Joint Research Programme ISJRP 138866, and Geneva University Hospital under grant PRD 11-II-1.

## REFERENCES

- [1] W. R. Hendee and E. R. Ritenour, *Medical Imaging Physics*, 4th ed. Hoboken, NJ, USA: Wiley, 2002.
- [2] X. Pan, E. Y. Sidky, and M. Vannier, "Why do commercial CT scanners still employ traditional, filtered back-projection for image reconstruction?" *Inv. Probl.*, vol. 25, no. 12, p. 1230009, 2009.
- [3] G. T. Herman, "Demonstration of beam hardening correction in computed tomography of the head," *J. Comput. Assist. Tomogr.*, vol. 3, no. 3, pp. 373–378, 1979.
- [4] K. Kitagawa, R. T. George, A. Arbab-Zadeh, J. A. Lima, and A. C. Lardo, "Characterization and correction of beam-hardening artifacts during dynamic volume CT assessment of myocardial perfusion," *Radiology*, vol. 256, no. 1, pp. 111–118, 2010.
- [5] W. A. Kalender, R. Hebel, and J. Ebersberger, "Reduction of CT artifacts caused by metallic implants," *Radiology*, vol. 164, no. 2, pp. 576–7, 1987.
- [6] M. Bazalova, L. Beaulieu, S. Palefsky, and F. Verhaegen, "Correction of CT artifacts and its influence on Monte Carlo dose calculations," *Med. Phys.*, vol. 34, pp. 2119–2132, 2007.
- [7] M. Abdoli, J. R. de Jong, J. Pruijm, R. A. J. O. Dierckx, and H. Zaidi, "Reduction of artefacts caused by hip implants in CT-based attenuation-corrected PET images using 2-D interpolation of a virtual sinogram on an irregular grid," *Eur. J. Nucl. Med. Mol. Imag.*, vol. 38, pp. 2257–2268, 2011.
- [8] M. Bal and L. Spies, "Metal artifact reduction in CT using tissue-class modeling and adaptive prefiltering," *Med. Phys.*, vol. 33, no. 8, pp. 2852–2859, 2006.
- [9] H. Yu, K. Zeng, D. K. Bharkhada, G. Wang, M. T. Madsen, O. Saba, B. Policeni, M. A. Howard, and W. R. K. Smoker, "A segmentation-based method for metal artifact reduction," *Acad. Radiol.*, vol. 14, no. 4, pp. 495–504, 2007.
- [10] H. Xue, L. Zhang, Y. Xiao, Z. Chen, and Y. Xing, "Metal artifact reduction in dual energy CT by sinogram segmentation based on active contour model and TV inpainting," in *Proc. IEEE Nuclear Science Symp. Conf. Rec.*, 2009, pp. 904–908.
- [11] C. Xu, F. Verhaegen, D. Laurendeau, S. A. Enger, and L. Beaulieu, "An algorithm for efficient metal artifact reductions in permanent seed implants," *Med. Phys.*, vol. 38, no. 1, pp. 47–56, 2011.
- [12] W. J. H. Veldkamp, R. M. S. Joemai, A. J. van der Molen, and J. Geleijns, "Development and validation of segmentation and interpolation techniques in sinograms for metal artifact suppression in CT," *Med. Phys.*, vol. 37, no. 2, pp. 620–628, 2010.
- [13] X. Zhang, J. Wang, and L. Xing, "Metal artifact reduction in X-ray computed tomography (CT) by constrained optimization," *Med. Phys.*, vol. 38, no. 2, pp. 701–711, 2011.
- [14] B. Meng, J. Wang, and L. Xing, "Sinogram preprocessing and binary reconstruction for determination of the shape and location of metal objects in computed tomography (CT)," *Med. Phys.*, vol. 37, no. 11, pp. 5867–5875, 2010.
- [15] J. Choi, K. S. Kim, M. W. Kim, W. Seong, and J. C. Ye, "Sparsity driven metal part reconstruction for artifact removal in dental CT," *J. X-ray Sci. Tech.*, vol. 19, pp. 457–475, 2011.
- [16] M. Meilinger, E. W. Lang, C. Schmidgunst, and O. Schutz, "Projective segmentation of metal implants in Cone Beam computed tomographic images," in *Proc. 7th Int. Symp. Image and Signal Processing and Analysis*, Dubrovnik, 2011, pp. 507–512.
- [17] M. Abdoli, M. R. Ay, A. Ahmadian, R. Dierckx, and H. Zaidi, "Reduction of dental filling metallic artefacts in CT-based attenuation correction of PET data using weighted virtual sinograms optimized by a genetic algorithm," *Med. Phys.*, vol. 37, pp. 6166–6177, 2010.
- [18] S. Zhao, D. Robertson, G. Wang, and B. Whiting, "X-ray CT metal artifact reduction using wavelets: An application for imaging total hip prostheses," *IEEE Trans. Med. Imag.*, vol. 19, pt. 12, pp. 1238–1247, Dec. 2000.
- [19] J. Gu, L. Zhang, G. Yu, Y. Xing, and Z. Chen, "X-ray CT metal artifacts reduction through curvature based sinogram inpainting," *J. X-ray Sci. Tech.*, vol. 14, no. 2, pp. 73–82, 2006.
- [20] Y. Zhang, Y. F. Pu, J. R. Hu, Y. Liu, Q. L. Chen, and J. L. Zhou, "Efficient CT metal artifact reduction based on fractional-order curvature diffusion," *Comput. Math. Meth. Med.*, p. 173748, 2011.
- [21] X. Duan, L. Zhang, Y. Xiao, J. Cheng, Z. Chen, and Y. Xing, "Metal artifact reduction in CT images by sinogram TV inpainting," in *Proc. IEEE Nuclear Science Symp. Conf. Rec.*, 2008, pp. 4175–4177.
- [22] Y. Zhang, Y. F. Pu, J. R. Hu, Y. Liu, and J. L. Zhou, "A new CT metal artifacts reduction algorithm based on fractional-order sinogram inpainting," *J. X-ray Sci. Tech.*, vol. 19, no. 3, pp. 373–384, 2011.
- [23] A. Mehranian, M. R. Ay, A. Rahmim, and H. Zaidi, "X-ray CT metal artifact reduction using wavelet domain sparse regularization," *IEEE Trans Med Imag.*, to be published.
- [24] M. Yazdi, M. A. Lari, G. Bernier, and L. Beaulieu, "An opposite view data replacement approach for reducing artifacts due to metallic dental objects," *Med. Phys.*, vol. 38, no. 4, pp. 2275–2281, 2011.
- [25] S. Tohna, M. A. J. M. Mahoney, and S. Crozier, "Dental CT metal artefact reduction based on sequential substitution," *Dentomaxillofac. Radiol.*, vol. 40, no. 3, pp. 184–190, 2011.

- [26] E. Meyer, R. Raupach, M. Lell, B. Schmidt, and M. Kachelrieß, "Normalized metal artifact reduction (NMAR) in Computed Tomography," *Med. Phys.*, vol. 37, pp. 5482–5493, 2010.
- [27] K. Y. Jeong and J. B. Ra, "Metal artifact reduction based on sinogram correction in CT," in *Proc. IEEE Nuclear Science Symp. Conf. Rec.*, 2009, pp. 3480–3483.
- [28] E. Meyer, R. Raupach, M. Lell, B. Schmidt, and M. Kachelrieß, "Frequency split metal artifact reduction (FSMAR) in computed tomography," *Med. Phys.*, vol. 39, no. 4, pp. 1904–1916, 2012.
- [29] J. Hsieh, *Computed Tomography: Principles, Design, Artifacts, and Recent Advances*, 2nd ed. Bellingham, WA: SPIE, 2009.
- [30] J. Nuyts and S. Stroobants, "Reduction of attenuation correction artifacts in PET-CT," in *Proc. IEEE Nuclear Science Symp. Conf. Rec.*, 2005, pp. 1895–1899.
- [31] M. Oehler and T. M. Buzug, "Statistical image reconstruction for inconsistent CT projection data," *Meth. Inf. Med.*, vol. 46, pp. 261–269, 2007.
- [32] B. De Man, J. Nuyts, P. Dupont, G. Marchal, and P. Suetens, "Reduction of metal streak artifacts in X-ray computed tomography using a transmission maximum a posteriori algorithm," *IEEE Trans. Nucl. Sci.*, vol. 47, no. 3, pp. 977–981, Jun. 2000.
- [33] L. Ritschl, F. Bergner, C. Fleischmann, and M. Kachelrieß, "Improved total variation-based CT image reconstruction applied to clinical data," *Phys. Med. Biol.*, vol. 56, pp. 1545–1561, 2011.
- [34] G. Van Gompel, K. Van Slambrouck, M. Defrise, K. J. Batenburg, J. de Mey, J. Sijbers, and J. Nuyts, "Iterative correction of beam hardening artifacts in CT," *Med. Phys.*, vol. 38, p. S36, 2011.
- [35] B. De Man, J. Nuyts, P. Dupont, G. Marchal, and P. Suetens, "An iterative maximum-likelihood polychromatic algorithm for CT," *IEEE Trans. Med. Imag.*, vol. 20, no. 10, pp. 999–1008, Oct. 2001.
- [36] J. F. Williamson, B. R. Whiting, J. Benac, R. J. Murphy, G. J. Blaine, J. A. O'Sullivan, D. G. Politte, and D. L. Snyder, "Prospects for quantitative computed tomography imaging in the presence of foreign metal bodies using statistical image reconstruction," *Med. Phys.*, vol. 29, no. 10, pp. 2404–2418, 2002.
- [37] H. Xue, L. Zhang, Y. Xing, and Z. Chen, "An iterative reconstruction technique for metal artifact reduction," in *Proc. 11th Int. Meet. Fully Three-Dimensional Image Reconstruction in Radiology and Nuclear Medicine*, 2011, pp. 199–202.
- [38] C. Lemmens, D. Faul, and J. Nuyts, "Suppression of metal artifacts in CT using a reconstruction procedure that combines MAP and projection completion," *IEEE Trans. Med. Imag.*, vol. 28, no. 2, pp. 250–260, Feb. 2009.
- [39] M. Abdoli, R. A. Dierckx, and H. Zaidi, "Metal artifact reduction strategies for improved attenuation correction in hybrid PET/CT imaging," *Med. Phys.*, vol. 39, no. 6, pp. 3343–3360, 2012.
- [40] K. Van Slambrouck and J. Nuyts, "Metal artifact reduction in computed tomography using local models in an image block-iterative scheme," *Med. Phys.*, vol. 39, no. 11, pp. 7080–93, 2012.
- [41] J. La Riviere, J. Bian, and P. A. Vargas, "Penalized-likelihood sinogram restoration for computed tomography," *IEEE Trans. Med. Imag.*, vol. 25, no. 8, pp. 1022–1036, Aug. 2006.
- [42] G. V. Gompel, K. V. Slambrouck, M. Defrise, K. J. Batenburg, J. D. Mey, J. Sijbers, and J. Nuyts, "Iterative correction of beam hardening artifacts in CT," *Med. Phys.*, vol. 38, no. S1, pp. S36–S49, 2011.
- [43] G. H. Chen, J. Tang, and S. Leng, "Prior image constrained compressed sensing (PICCS): A method to accurately reconstruct dynamic CT images from highly undersampled projection data sets," *Med. Phys.*, vol. 35, no. 2, pp. 660–3, 2008.
- [44] V. Cevher, A. Sankaranarayanan, M. F. Duarte, D. Reddy, R. G. Baraniuk, and R. Chellappa, "Compressive sensing for background subtraction," in *Proc. 10th Eur. Conf. Computer Vision: Part II*, Marseille, France, 2008, pp. 155–168.
- [45] D. Prell, Y. Kyriakou, M. Beister, and W. A. Kalender, "A novel forward projection-based metal artifact reduction method for flat-detector computed tomography," *Phys. Med. Biol.*, vol. 54, no. 21, p. 6575, 2009.
- [46] B. Kratz, I. Weyers, and T. M. Buzug, "A fully 3D approach for metal artifact reduction in computed tomography," *Med. Phys.*, vol. 39, no. 11, pp. 7042–7054, 2012.
- [47] P. Perona and J. Malik, "Scale-space and edge detection using anisotropic diffusion," *IEEE Trans. Pattern Anal. Mach. Intell.*, vol. 12, no. 7, pp. 629–639, Jul. 1990.
- [48] K. Lange, D. R. Hunter, and I. Yang, "Optimization transfer using surrogate objective functions," *J. Comput. Graph. Statist.*, vol. 9, pp. 1–20, 2000.
- [49] A. Beck and M. Teboulle, "Gradient-Based Algorithms with Applications in Signal Recovery Problems," in *Convex Optimization in Signal Processing and Communications*, D. Palomar and Y. Eldar, Eds. Cambridge, U.K.: Cambridge Univ. Press, 2010, pp. 33–88.
- [50] E. P. Chong and S. H. Zak, *An Introduction to Optimization*, 2nd ed. Hoboken, NJ, USA: Wiley, 2001.
- [51] J. Dahl, P. C. Hansen, S. H. Jensen, and T. L. Jensen, "Algorithms and software for total variation image reconstruction via first-order methods," *Numer. Alg.*, vol. 53, pp. 67–92, 2010.
- [52] A. Beck and M. Teboulle, "A fast iterative shrinkage-thresholding algorithm for linear inverse problems," *SIAM J. Imag. Sci.*, vol. 2, no. 1, pp. 183–202, 2009.
- [53] S. Karimi, P. Cosman, C. Wald, and H. Martz, "Segmentation of artifacts and anatomy in CT metal artifact reduction," *Med. Phys.*, vol. 39, no. 10, pp. 5857–68, 2012.
- [54] P. J. La Riviere, "Penalized-likelihood sinogram smoothing for low-dose CT," *Med. Phys.*, vol. 32, no. 6, pp. 1676–1683, 2005.
- [55] G. Poludniowski, G. Landry, F. DeBlois, P. M. Evans, and F. Verhaegen, "SpekCalc: A program to calculate photon spectra from tungsten anode X-ray tubes," *Phys. Med. Biol.*, vol. 54, no. 19, p. N433, 2009.
- [56] M. J. Berger and J. H. Hubbell, "XCOM: Photon cross sections on a personal computer," Center for Radiation Research, National Bureau of Standards, 1987.
- [57] B. De Man, J. Nuyts, P. Dupont, G. Marchal, and P. Suetens, "Metal streak artifacts in X-ray computed tomography: A simulation study," in *Proc. IEEE Nuclear Science Symp. Conf. Rec.*, 1998, pp. 1860–1865.
- [58] J. Fessler, *Image Reconstruction Toolbox*, Univ. Michigan [Online]. Available: <http://www.eecs.umich.edu/~fessler/code/index.html>, Accessed 2012
- [59] C. Lemmens, M.-L. Montandon, J. Nuyts, O. Ratib, P. Dupont, and H. Zaidi, "Impact of metal artefacts due to EEG electrodes in brain PET/CT imaging," *Phys. Med. Biol.*, vol. 53, no. 16, pp. 4417–4429, 2008.
- [60] Y. Chen, Y. Li, H. Guo, Y. Hu, L. Luo, X. Yin, J. Gu, and C. Toumoulin, "CT metal artifact reduction method based on image segmentation and sinogram in-painting," *Math. Prob. Eng.*, vol. 2012, 2012, Article ID 786281, 18 pages.
- [61] F. Morsbach, S. Bickelhaupt, G. A. Wanner, A. Krauss, B. Schmidt, and H. Alkadhi, "Reduction of metal artifacts from hip prostheses on CT images of the pelvis: Value of iterative reconstructions," *Radiology*, 2013, in press.
- [62] Y. Zhang, H. Yan, X. Jia, J. Yang, S. B. Jiang, and X. Mou, "A hybrid metal artifact reduction algorithm for X-ray CT," *Med. Phys.*, vol. 40, no. 4, pp. 041910–17, 2013.
- [63] O. Sadowsky, L. Junghoon, E. G. Sutter, S. J. Wall, J. L. Prince, and R. H. Taylor, "Hybrid cone-beam tomographic reconstruction: Incorporation of prior anatomical models to compensate for missing data," *IEEE Trans. Med. Imag.*, vol. 30, no. 1, pp. 69–83, Jan. 2011.
- [64] R. M. S. Joemai, P. W. D. Bruin, W. J. H. Veldkamp, and J. Geleijns, "Metal artifact reduction for CT: Development, implementation, and clinical comparison of a generic and a scanner-specific technique," *Med. Phys.*, vol. 39, no. 2, pp. 1125–1132, 2012.